A TEST OF WVR-BASED TROPOSPHERE CALIBRATION USING VLBI OBSERVATIONS ON A 21 KM BASELINE

by

R. P. Linfield, S. J. Keihm, 1,. P. Teitelbaum, S. J. Walter,

M. J. Mahoney, R. N. Treuhaft, L. J. Skjerve

Jet Propulsion Laboratory

California Institute of Technology

Oct. 13, 1994

ABSTRACT

Simultaneous VLBI and WVR measurements on a21 km baseline showed that calibration by WVRs removed 8090% of the effect of tropospheric delay fluctuations for these experiments. From comparison of the residual delay variations within scans and between scans, the total tropospheric contribution to the delay residuals for each of the three 5-20 hr sessions was estimated as 1 1%, 16%, and 17%, with the first value being very uncertain. The observed improvement in *rms* residual delay from WVR calibration during these three sessions was 1 %, 13%, and 18910, respectively; these improvements from WVR calibration indicate that 80-90% of the fluctuations were removed. The improvement is consistent with the estimated 2--3 mm path delay precision of current WVRs. The VLBI measurements, of natural radio sources, were conducted in April and May, 1993 at Goldstone, California. Dual frequency (2.3 and 8.4 GHz) observations were employed to remove the effects of charged particles from the data. Measurements with c-pointed Water Vapor Radiometers (WVRs), located within 50 m of the axis of each antenna, were performed to test the ability of the WVRs to calibrate line of sight path delays. Factors which made WVR performance assessment difficult included 1) the fact that the level of tropospheric fluctuations was smaller than is typical for Goldstone during these experiments, and 2) VLBI delay variations on longer time scales (*i. e.* over multiple scans) contained uncalibrated instrumental effects (probably a result of slow temperature variations in the VLBI hardware) that were larger than the tropospheric effects.

I. INTRODUCTION

Ground-based observations at radio frequencies of compact natural radio sources or spacecraft can yield highly accurate position or velocity measurements. Very Long Baseline Interferometry (VLBI) measures the relative delay in arrival time of wavefronts from a source at two or more sites. Spacecraft range and Doppler tracking measure the delay, or its time derivative, of a round trip radio signal transmitted between the ground and the spacecraft. In order to extract an angular position from a VLBI delay, a distance from a range measurement, or a radial velocity from a Doppler measurement, non-geometric components of the delay/delay rate must be removed. Many of these delay error sources can be estimated from VLB1 data, provided that the functional form of the delay signatures of the error sources is known, and that these functional forms are significantly different fi orn those induced by source angular position shifts. As an example, a clock offset and a linear (in time) clock rate can be estimated (and subtracted) from VLBI observations if multiple sources are observed, or if one source is observed for an extended period of time,

The troposphere contributes approximately 7 nsec of delay at the zenith, equivalent to a path length increase of $\Delta l_{zen} \approx 2,1$ m. (Hereafter, whenever a length is given for a delay, the delay in time units is that length divided by the speed of light). At an elevation angle 6, the effective path length increase is $\approx \mathrm{Al}_{zen}/\sin\theta$. One can solve for the mean tropospheric zenith delay over some period of time by using a mapping function to relate the delay $\tau(\theta)$ at elevation angle θ to the zenith delay $\tau_{z\,en}$ $(\tau(\theta) = \tau_{zen}/\sin\theta$ is an approximate mapping function). Because of inhomogeneities in tropospheric refractivity,

3

clue primarily to inhomogeneities in water vapor density, estimating and subtracting such a mean troposphere will still leave a residual tropospheric delay which will corrupt the data.

The residual tropospheric delay was the largest error source in the astrometric VLB1 observations of Treuhaft and Lowe (1991), who were able to reduce the effects of the troposphere to ~ 1 cm on a 10000 km baseline. This corresponds to an angular error of ~ 1 nanoradian (nrad), or 200 microarcseconds over angular scales of 30° on the sky. In order to achieve angular accuracies better than 1 nrad with VLBI, direct calibration of tropospheric delay is required. A sufficiently accurate line-of-sight delay calibration would enable substantial improvements in the accuracy of VLBI and spacecraft Doppler tracking measurements.

Because water vapor accounts for nearly all the small scale structure in refractivity at microwave frequencies, efforts to calibrate line-of-sight delay have focused on measurements of water vapor. Water Vapor Radiometers (WVRs) measure thermal emission from water vapor at microwave frequencies. In order' to test WVR wet delay calibration techniques, we designed and conducted a short baseline VLBI experiment.   By using a short baseline (21 km, instead of the 300 0–1 0000 km baselines typically used for astrometric VLBI), many non-tropospheric error sources were greatly reduced. Any geophysical modeling errors at each antenna cancel nearly perfectly over such a short baseline. Source position and earth rotation/orientation errors result in very small delay errors. The short baseline allowed the use of the VLBI phase delay data type (described in Section IV), greatly reducing the thermal noise level. We

4

expected tropospheric and instrumental (VLBI hardware) effects to be the two largest contributions to the measured residual delays.

11. WET TROPOSPHERE CALIBRATION

A. Wet Delay Formulation

The effect of the atmosphere on the propagation of a microwave signal, expressed as a range correction, or path delay τ, is the difference between the electrical and geometric path lengths:

$$(1) \qquad \tau = \int_0^\infty (n-1)ds = 10^{-'} \int_0^\infty N(s)ds$$

Here n is the refractive index, N is the refractivity, defined as the difference between the refractive index and unity, in parts per million, and the integrals are evaluated along the line of sight path through the atmosphere..

The refractivity is typically expressed as the sum of "dry" (hydrostatic) and "wet" (water vapor-induced) components (Elgered, 1993) in which the dry component depends only on the total density and the wet component depends on water vapor density ρ_v and physical temperature T. Using the formulation of Thayer (1974), the wet refractivity component N_{wet} can be expressed as

$$(2) \qquad N_{wet} = \left(K_1 \rho_v + K_2 \frac{\rho_v}{T} \right) Z_w^{-1}$$

Z_w, which accounts for non-ideal gas behavior, has a value of 1.0 within 2×10^{-3} for atmospheric conditions (Owens, 1967). Using the laboratory measurements

5

of Boudouris (1963) for the constants K_1 and K_2, the wet delay τ_{wet} can be expressed as

$$(3) \qquad \tau_{wet} = 10^{-6} \int_O^\infty \left(0.1095/)_0 + 1733\frac{\rho_v}{T}\right) ds$$

Here ρ_v is in units of g/m^3, T is in Kelvins, and τ_{wet} is in seconds.

Extensive evaluation (Hill et al., 1982) of the theoretical and experimental determinations of the vapor-induced refractivity component indicates that the relationship expressed in Eq. (3) is accurate at the 0.5% level. At microwave frequencies below 30 GHz, the wet refractivity component is practically non-dispersive and the wet delay can be considered frequency-independent.

B. WVR Measurements of the Wet Delay

Measurement of therms] emission from the optically thin 22 GHz water vapor spectral line is one potential method for calibrating the line-of-sight wet delay. A water vapor radiometer (WVR) measures sky brightness temperatures T_b at one or more frequencies near the 22 GHz peak, with an additional channel above 30 GHz to correct for emission from liquid water when clouds are present (e.g. Elgered, 1993). Portable W VRS are steerable in both azimuth and elevation and typically have Half Power Beam Widths (HPBW) of 6°–90.

WVR calibration is achieved by the use of an ambient reference target and tipping curves for system gain determination. During tip curve operations, WVRs obtain sky measurements over a range of elevation angles and utilize an extrapolation to zero air mass M (A4 $\equiv$ 1 / sin θ, where θ is the elevation angle) to establish the' cosmic background temperature as the cold reference.

6

The tip curve calibration method produces absolute brightness temperatures with accuracies < 1 K and precisions < 0.1 K for hour time scales. For periods during which tip curves are not available (*e.g.* during VLBI tracking), gain variations are estimated through their correlations with instrument temperatures. These correlations are established by one day or more of prior tip data.

The link between measured WVR brightness temperature T_b and atmospheric properties is provided by the standard microwave equation of radiative transfer for a non-scattering medium in local thermodynamic equilibrium (Chandrasekhar, 1950):

$$(4) \qquad T_b = \int_0^\infty T(s)\alpha(\rho_v, T, P)e^{-\tau(s)}ds + T_{MB}e^{-\tau(\infty)}$$

The optical depth, $\tau(s)$, is

$$(5) \qquad T(S) = \int_0^S \alpha(\rho_v, T, P)ds$$

In Eqns. (4) and (5), $\alpha(\rho_v, T, P)$ is the volume absorption coefficient, including contributions from molecular oxygen, water vapor, and suspended cloud liquid (when present). The absorption depends upon the water vapor density ρ_v (and liquid density when clouds are present), the temperature T, and the pressure P, each of which in turn is a function of position along the line-of-sight path. T_{MB} is the blackbody temperature of the cosmic microwave background radiation.

For clear-sky conditions, WVR brightness temperature T_b and the wet path delay τ_{wet} are highly correlated, because both are approximately proportional to the integrated water vapor content along the line of sight. 'This correlation has been demonstrated in a number of experiments which compared WVR-derived path delays to direct measurements with weather balloons (Westwater *et al.*, 1990; England *et al.*, *1993)* and inferred values from GPS measurements (Lichten, 1990; Tralli and Lichten, 1990).

Given a set of WVR brightness temperature measurements, the vapor-induced path delays are usually computed from a statistical retrieval (e.g. Gary *et* al., 1985). Atmospheric profiles measured by radiosonde flights at selected sites are used to generate a computational data base of path delays and corresponding WVR brightness temperatures for a wide range of atmospheric conditions. Two or more years of twice-daily radiosonde profiles are typically used to characterize site conditions. A linear fit to the database produces an equation relating path delay to WVR brightness temperatures. For typical WVR measurement errors of 0.5 K, formal errors for retrieved zenith path delay of 2--3 mm are commonly obtained. This corresponds approximately to a 2--3% error for calibration of average ($\approx$ 10 cm) zenith wet path delays at sites used for spacecraft tracking. Other WVR wet path delay errors are described in section IIC.

Independent wet delay calibration must be highly accurate in order to improve the accuracy of VLBI astrometric or spacecraft Doppler measurements. (Spacecraft range measurements are currently limited by calibration uncertainty in the delays through electronics, rather than by the troposphere.) VLBI astrometric measurements can be used to determine line-of-sight tropospheric

delay to within ≈ 1 cm (Treuhaft and Lowe, 1991). The line-of-sight wet delay for an elevation angle of 15° is typically 30–70 cm, so a calibration precision (if not accuracy) of $\sim 1\%$ is needed in order to improve the accuracy of astrometric VLBI or Doppler data. A precision several times better than 1% is desired. Although WVRs have been tested against radio interferometric measurements previously (Resch *et al.*, 1984; Edwards, 1990), wet delay calibration at the 1% level has never been demonstrated. The purpose of our observations was to find the limiting errors for such a demonstration.

C. Error Sources in WVR Measurements of Wet Path Delay

The 2-3 mm formal error in WVR-derived zenith wet delay stated in section IIB includes only the effects of 0.5 K WVR "noise" and the variability of temperature and vapor height distribution. The formal error represents the *rms* accuracy that one would expect for WVR measurements with zero bias, a perfect absorption model, and a pencil beam. In applying WVR measurements as wet delay corrections for other instruments, a number of other error sources, must be considered:

(1) Unmonitored gain variations

WVR measurement errors are not properly characterized as pure noise with zero bias. The most serious instrumental uncertainty is due to unmonitored gain variations over time scales of minutes-hours, due primarily to temperature variations of the WVR electronic components. For the WVRs used in this experiment, gain variations were monitored to the 0.05-0.1% level, either by estimating the gain from its strong correlation with mixer temperature measured during tip curve calibration, or by time

interpolation between tip curve data obtained before and after the VLBI observations. A 0.1 % gain uncertainty corresponds to a 0.3 K WVR measurement error and a 1-2 Inm uncertainty in the retrieved wet delay.

(2) **WVR elevation pointing errors**

WVR pointing errors can be significant at low elevation angles where brightness temperature varies most strongly with airmass. For the extremely dry conditions encountered at Goldstone during our observations, at 30°, the lowest WVR elevation angle employed, WVR brightness temperatures decrease by approximately 1 K for an elevation increase of 10. For elevation uncertainties $\sim 0.3°$, typical of the Goldstone WVRS, the net effect on the wet delay retrieval error is $\leq$ 1-2 mm at $\geq$ 30° elevation angle.

(3) **Vapor absorption model error**

The absolute uncertainty in any single measurement of WVR-derived wet delay is normally dominated by the 5% uncertainty (Keihm, 1992) in the adopted vapor absorption model which links measured brightness temperatures to integrated vapor and path delay. For the dry Goldstone conditions, with average zenith wet delays of ~ 5 cm, this absolute error component is 2-3 mm. However, its effect was <1 mm, because the role of the WVRS in this VLBI experiment was to monitor the *difference* in delay between two sites, and the line-of-sight wet path delays at the two sites were similar.

(4) **Beam offset and mismatch errors**

The expected differences between wet delays sensed by WVR and DSN antennas depend on integration t ime, elevation angle, and the beam mismatch and beam axis offset between the instruments. For the Goldstone

10

experiment, WVRs with conical 6 9° HPB W beams were deployed ≈ 50 m from the DSS 13 (26 m diameter) and DSS 15 (34 m diameter) antennas. Both of the DSN antennas have essentially cylindrical beams in the troposphere. Based on a turbulence model for the troposphere (Treuhaft and Lanyi, 1987), the expected delay difference between the WVR and DSN beams for integration times >2 min. and elevation angles >20° is <0.15 mm (Linfield and Wilcox, 1993).

D. Additional Instrumentation

The formal or "inherent" WVR path delay retrieval error of 2–3 mm, described in section IIB, is due primarily to variations of air temperature and water vapor density along the line of sight, To calibrate this error, additional instrumentation was deployed at Goldstone for the VLBI/WVR experiment. At DSS 15 a Microwave Temperature Profiler (MTP) (Denning et al., 1989) was deployed. Using elevation scanning measurements near the 60 GHz 0_2 absorption band, the MTP provides atmospheric temperature profile data with accuracies of 1–2 K for altitudes below 3 km (Westwater, 1993), where most of the water vapor resides.

In order to characterize the state of the atmosphere during the observations and to obtain independent site measurements of the vertical temperature and vapor density profiles, radiosondes were launched approximately every six hours. Our launch sites were 200–400 m from each antenna. Comparisons of the radiosonde measurements near the ground with measurements made by co-located surface sensors indicated that the radiosonde temperature and pressure

measurements were accurate to $1°C$ and 3 mbar, respectively. However, similar comparisons revealed large and variable discrepancies in relative humidity measurements. We were thus unable to improve WVR path delay retrievals by constraining the relative height distribution of the vapor. The radiosonde data did, however, provide validation for the MTP measurements of lower troposphere temperature profiles. In addition, optical tracking of radiosonde flights at DSS 13 provided measurements of wind velocity and direction as a function of altitude. These measurements were used in modeling the magnitude of tropospheric turbulence effects on our VLBI data.

III OBSERVATIONS AND DATA REDUCTION

A. VLBI

We conducted six VLBI observing sessions; their dates and durations are given in Table 1. We used two antennas of NASA's Deep Space Network in Goldstone, California: DSS 13 (26 m diameter) and DSS 15 (34 m diameter). The two antennas are separated by 21.3 km along azimuth 313° (DSS 15 is north and west of DSS 13).

In addition, we observed with a 34 m diameter antenna (DSS 65) in Madrid, Spain during the first 24 hr of session 3 and with a 34 m diameter antenna (DSS 45) in Canberra, Australia during all of session 4. Time on the DSS 15-DSS 65 baseline in session 3 and the DSS 15-- DSS 45 baseline in session 4 had been previously allocated for astrometric VLBI observations. For these two sessions, we used the observing schedules created for those observations.

These schedules were designed to provide geometric strength (i.e. allow the separation of baseline, source position, and tropospheric effects) on long baselines. The schedules emphasized 2-4 observations of each source, with each observation typically near rise, set, or transit at one of the two stations, Only results on the DSS 13- DSS 15 baseline are reported in this paper.

For the other four 5-7 hr sessions, our observing schedule was modified from an astrometric VLBI schedule to use stronger sources and have elevation angles $> 30°$ (thus allowing the co-pointing of WVRs, which cannot point below 30° without significant ground contamination of the measured brightness temperatures). In addition, we scheduled some long scans (300 700 s) on strong sources (typical scans were ≈ 150 s in length).

All VLBI observations used the Mk III recording system (Rogers $et\,al.$ 1983) in mode C, with five 2 MHz channels spanning 2200-2300 MHz (S-band) and nine 2 MHz channels spanning 8215-8583 MHz (X-band). Using two observing bands allows a calibration of the dispersive delay due to charged particles in the earth's ionosphere and the interplanetary medium. (For an observing frequency ν well above the plasma frequency, the charged particle delay is proportional to V^{-2}.)

After each 2 MHz channel was mixed to baseband, it was sampled at the Nyquist rate, digitized to one bit, and recorded on tape. In addition, the digitized data from DSS 15 were sent over optical fiber to DSS 13, where the DSS13-DSS 15 baseline was correlated with the real-time Block II correlator (Edwards et al. 1992), The correlated data were written to disk for later processing. The results presented in this paper are based upon data correlated in real time at DSS 13.

13

As a test of the accuracy of the real-time correlator, the data recorded on tape during Session 5 were correlated with the JPL/CIT Block II correlator. The quality of tape playback was poor, and only 53 scans could be decoded. The difference between the S/X group delays from the two correlators had a mean of 155 psec and a standard deviat ion of 3,5 psec. The mean offset is thought to be due to details in the application of manual phase calibration in the post-processing routine FIT (Lowe, 1992). Because this offset looks exactly like a clock offset, it will not affect later results. The 3.5 psec *rms* is due at least in part to the poor quality of tape playback. However, even if it were due entirely to errors in the real-time correlator, it would be too small to significantly affect the results presented in Section V.

In order to calibrate the variation of instrumental delays with frequency and time, phase calibration was used at each antenna. Phase calibration tones were injected between the feed horn and the first stage RF amplifier, and later extracted by the correlator for use in correcting interferometric delays. At DSS 15, a phase calibration unit with a cable stabilizer (Sigman, 1987) was used. This stabilizer greatly reduces the effect of path length changes between the hydrogen maser frequency standard on the ground and the tone generator at the feed horn.   The entire system has an estimated error of $\leq$ 10 psec over 24 hr due to diurnal temperature changes. Over time scales $\leq$ 6 hr, the nonlinear delay errors were several times smaller than 10 psec. At DSS 13, the phase calibration unit did not have cable stabilization, and the instrumental delay calibration errors were therefore larger (this is discussed further in Section VI).

14

The post-processing routine FIT was used to extract the residual phase from the correlated data for each scan, along with the derivatives of this phase with respect to frequency (group delay) and time (phase rate). The values of these quantities from the correlator model were added to the residual values to obtain total observable. The total phase produced in this way contained integer cycle ambiguities. These were resolved by a technique described in Section IV. When the integer cycle ambiguities were removed, the phase delay τ_{ph} could be calculated as $\tau_{ph} = \phi/\nu_{avg}$, where ϕ is the total phase at a mean observing frequency ν_{avg}.

B. WVRS

During each of the six VLB1 sessions WVRs were deployed near each of the two Goldstone antennas A J-series WVR (J3) (Janssen, 1985) was located 50 m north of the DSS 13 azimuth axis, and a D-series WVR (D2) (Keihm, 1991) was located 40 m south of the DSS 15 azimuth axis. Both WVRs observed simultaneously in two channels, 20.7 and 31.4 GHz, with effective bandwidths of 320 MHz. The J3 instrument also has a 22.2 GHz channel (at the peak of the water vapor line), but this channel was not used during our observations. The estimated thermal noise level for 5–6 s integrations was approximately 0.06 K for D2 and 0.10 K for J3, corresponding to path delay errors of ≈ 0.4 mm (D2) and ≈ 0.6 mm (J3). Thermal WVR noise was not a limiting error source in this experiment,

During VLB1 source measurements, the WVRs were co-pointed with the DSS 13 and DSS 15 antennas whenever viewing conditions allowed. However,

unlike the two large radio antennas. the WVRS observed in a constant direction during a scan. Neither WVR was capable of taking data while slewing. The WVR 6°-9° beams arc subject to significant sidelobe pickup whenever a substantial obstruction lies within $\sim 20°$ of the beam axis. Prior to the experiment, the WVRS were operated in a horizon scanning mode to establish the azimuth-dependent minimum elevation angles free of ground pickup. For most observations and azimuths, 30° was chosen as a safe elevation angle lower limit. At 1)SS 15, where the D2 WVR sat on the ground to the south and substantially below the VLBI antenna, elevation angles <75° were precluded for source azimuths in the range (– 45°, +450).

While performing line-of-sight measurements during VLBI scans, both WVRS observed the sky nearly continuously, with 6 s interruptions once per minute to measure a reference load. The J3 WVR observed this load by internal switching, while the D2 unit slewed its antenna away from the radio source line of sight to an external ambient target. During gaps of two or more minutes between VLBI source measurements, the WVRs performed tip curves to monitor gain variations. For the J3 unit, the tip curves obtained during the VLBI observing gaps provided interpolation points for gain calibration during the six-hour sessions. For the D2 unit, calibration variations were tracked using an empirical correlation between gain and mixer temperature established from tip curve data obtained prior to and following the VLBI observing sessions. The D2 tip curves obtained during gaps within the VLBI observing sessions provided a check on the precision of the mixer temperature gain tracking technique.

IV. ANALYSIS

Data from the first three sessions were not usable for subsequent analysis. During session 1, instrumental phase calibration was not available at DSS 13. During session 2, hardware problems caused the loss of a large fraction of the VLBI data and most of the WVR data. During session 3, technical problems caused the instrumental phase calibration at DSS 13 to be too noisy to use. The number of useable scans, defined as having working phase calibration, adequate SNR for phase connection (discussed below), and valid WVR data from both DSS 13 and DSS 15, are given for all six sessions in Table 2.

A. Calculating VLBI Phase Delays

The extraction of total VLBI delays for each scan at both S and X-band was described in Section 111A. The one standard deviation (1σ) thermal noise $\Delta\tau_{SNR}$ in delay measurements, due to limited signal-to-noise ratio (SNR) in the data, is approximately

$$(6) \qquad \Delta\tau_{SNR_g} \approx \frac{\sqrt{2}}{2\pi\Delta\nu_{span}\ SNR} \qquad \text{for group delay}$$

$$(7) \qquad \Delta\tau_{SNR_{ph}} \approx \frac{1}{2\pi\nu_{avg}\ SNR} \qquad \text{for phase delay}$$

$\Delta\nu_{span}$ is the spanned bandwidth at X-band (368 MHz) and ν_{avg} is the mean X-band observing frequency (8405 MHz). SNR is the signal-to-noise ratio for the entire scan, when all nine X-band frequency channels are combined. The derivation of eqs. (6) and (7) follows from the fact that, for thermal noise, the phase error (in radians) of a complex value is equal to the fractional amplitude

error. Although the measured 'charged particle free' delays are linear combinations of S- and X-band delays, the errors are dominated by the X-band delay errors because the X-band delay weights in the linear combination are a factor of $(\nu_X/\nu_S)^2 \approx 14$ times larger than the S-band weights.

The values of $\Delta\tau_{SNR_g}$ ranged from $<$ 1 picosecond (psec) to $>$30 psec, with $\Delta\tau_{SNR_g} \geq 10$ psec for many scans. Because the goal of this experiment was to look for mm-level effects (1 mm corresponds to ≈ 3 psec), we used the phase delay observable τ_{ph}.

$$\tau_{ph} \equiv \frac{\phi}{\nu_{avg}}$$

Here #J is the total phase in cycles, including integer cycles, at the mean X-band frequency ν_{avg}. Use of the phase delay reduced $\Delta\tau_{SNR}$ a factor of ≈ 20 below that for the group delay.

The group delays were used to resolve integer cycle ambiguities (i.e. to 'connect phase' from one scan to the next) in the phase delays. In order for this to be accomplished, the thermal noise in the group delays had to be sufficiently small that the probability of making a cycle error was negligible. If we set a 5σ threshold for a cycle error (defined as an error in the group delay of $>$0.5 cycle), then

$$\Delta\tau_{SNR_g} < \frac{0.1}{\nu_{avg}}$$

This leads to

$$SNR > \frac{10\sqrt{2}\nu_{avg}}{2\pi\Delta\nu_{\text{span}}}$$

For S- and X-band, the constraints on SNR are

$$SNR_S \; >51$$

18

$$SNR_\mathrm{X} > 51$$

Because charged particles affect group and phase delays with opposite signs, it was not possible to perform phase connection using raw delays. The following procedure was used. First, the S- and X-band group delays were used to derive a 'charged particle free' group delay $\tau_g(S/X)$ and an electron column density N_g. The accuracy of both quantities was limited by thermal noise in the group delays. Second, N_g was used to remove most of the charged particle contribution. to the S- and X-band phase delays. Using τ_g (S/X), the integer cycle ambiguities in these phase delays were determined. The corrected phase delays were then used to estimate charged-particle free phase delays $\tau_{ph}(S/X)$, which were used for subsequent analysis,

B. VLBI Parameter Estimation

The charged-particle-free phase delays for each observing session were an-alyzed using JPL's program MODEST (for MODel and ESTimation) (Severs 1991). First, an *apriori* model delay was subtracted from each scan. This : model included atmospheric, source, baseline, relativistic, and geophysical pa-rameters. For the short baseline in this experiment, many components of this model gave negligible contribution. The dominant components of the model consisted of 1) a geometric term, based on UT1 (i.e. universal time corrected for earth rotation irregularities UT1 $-$ UTC), station locations for the two an-tennas, and source positions converted from J2000 to date via precession, nu-tation, and aberration, and 2) a media term, consisting of tropospheric delay differences. The *apriori* differential dry zenith delays were derived from surface pressures at the two antennas and the elevation angles of the sources. For our

19

apriori model of wet delay differences, we used either zero (i.e. no calibration) or the station-differenced line of sight WVR wet path delay estimates. Both options were used for all sessions so that the effectiveness of WVR calibration could be quantified.

The model subtraction produced a set of residual delays. The estimation process did a least squares fit to these residuals, solving for two or more parameters. In all cases, two clock parameters, a delay offset and a linear delay rate, were estimated. Other parameters estimated during some runs were a residual mean zenith troposphere difference and a correction to the baseline vector between the two antennas.

The clocks at the two antennas were derived from the same frequency standard, However, the cable lengths distributing this standard to the two antennas were different, so that the mean difference clock value at the two antennas was nonzero. Furthermore, not all parts of this distribution system were compensated for path length changes, so that a small nonzero clock rate was expected (our fitting yielded values of $10-*5-10^{-14}$ s/s). These two parameters reduced the *rms* scatter among the residuals (i.e. the *interscan* residuals) to <30 psec for Sessions 5 and 6, and ≈ 70 psec for Session 4. With two clock breaks (i.e. discontinuities in the magnitude and first derivative of the parameters describing the offset) inserted into Session 4 during fitting, the residuals dropped to < 30 psec. These clock breaks are an approximate way of dealing with nonlinear instrumental delay changes over long time scales (24 hours for Session 4).

The residual mean zenith troposphere difference parameter primarily rep resented the session-averaged difference in the wet delays (DSS 15 consistently

20

had a larger wet delay than DSS 13). However, it also accounted for any calibration error in the dry delay difference between the two sites.

For session 4, where there were a large number of scans with broad sky coverage, an attempt was made to solve for a correction to the vector baseline between the two antennas. However, solving for these additional three parameters resulted in minimal reduction to the *interscan* residuals. For all results reported below, the baseline was left unchanged from its *apriori* value, derived from multiple previous VLBI observations.

Because most or all VLBI astrometric and geodetic results have been based on group delays, we checked for possible systematic errors in the calculation and treatment of phase delays. Group delays were used in comparison runs of MODEST for Sessions 5 and 6, both with and without WVR calibration. The resulting VLB1 *interscan* residual delays were equal, in all cases, to the residual phase delays with ≈ 10 psec of noise added in quadrature. We conclude that any systematic errors in the phase delays were much less than 10 psec.

C. WVR-Based Delay Residuals

Site differenced line-of-sight wet delays were determined from the WVR data at ≈ 6 s intervats for each VLBI source observation. Because the WVRs, and DSN antennas could not always be co-pointed, the two-channel line-of-sight WVR brightness temperature were first converted to zenith-equivalent brightness temperatures using the effective radiating temperature approximation to eq. (4) (Elgered, 1993):

$$(8) \qquad\qquad T_b(M) = T_{eff} - (T_{eff} - T_{MB})\, e^{-\tau(M)}$$

The value of T_{eff} used was 285 K. T_{MB} is the cosmic background microwave temperature, and M is the airmass ($M \equiv 1 / \sin\theta$, where θ is the elevation angle). Given a value for $T_b(1)$ (*i.e.* T_b at the zenith), $\tau(1)$ can be computed and the path delay can be accurately mapped to any other elevation angle >15° using the relation $\tau(M) = \tau(1) / \sin\theta$.

Once converted to zenith, the WVR brightness temperatures were used to determine zenith path delay. A linear retrieval algorithm was based on correlations between Desert Rock, Nevada radiosonde measurements of zenith path delay and computed WVR brightness temperatures. The brightness temperatures were generated from the radiosonde data using the modified Liebe vapor absorption model (Keihm, 1992). Desert Rock is considered the site equivalent of Goldstone, both in altitude and average moisture content. The path delay retrieval algorithm generates three path delay values for each input set of WVR zenith brightness temperatures one using both channels and one each using the channels independently. For most operating conditions the two-channel algorithm provides the most accurate path delay results. For time intervals under cloudless conditions for which the behavior of one channel is anomalous or subject to larger than normal gain uncertainties, the single channel algorithms can be applied using data from the more reliable channel, Other algorithms, which augmented the WVR data with MTP measurements of the lower troposphere temperature profile, were also tried, but produced no additional reduction in the final VLBI site-differenced residuals.

When the WVR data were included in the VLBI processing, the derived zenith WVR delays were mapped to the DSN antenna elevation for each pass,

If no obstructions precluded co-pointing, the mapping coincided with the original WVR pointing. These data are considered the highest quality WVR measurements of path delay correction and were assigned a quality flag of 3. If co-pointing did not occur but the WVR and VLBI antennas were aligned within one WVR HPBW (70), then a quality flag of 2 was assigned. If there was some indication of WVR ground pickup of magnitude < 1 K, then a quality flag of 1 was assigned. With evidence of ground pickup exceeding 1 K or any indication of anomalous WVR calibration behavior, the quality flag was set to O. For all results reported in the following section, only quality flag ≥ 2 data were utilized. This data comprised $\approx 70\%$ of the passes of VLBI observation sessions 4, 5, and 6.

V. RESULTS

A. Interscan Delay Residuals

The results of the MODEST runs for Session 4-6 are summarized in Tables 3 and 4. Results *without* VLBI troposphere estimation are listed in Table 3; results *with* VLBI troposphere estimation are listed in Table 4. All entries in these tables correspond to VLBI scan-averaged phase delay residuals. Column 3 in each table gives *rms* VLBI *interscan* post-fit delay residuals when WVR line-of-sight wet path delay estimates were applied as calibration. These estimates use two channel (20.7 and 31.4 GHz) retrievals for the J-WVR and one channel (31.4 GHz) retrievals for the D-WVR. other combinations were also tried, but gave inferior results. As discussed below, the D2 channel 1 data

were apparently corrupted by instrument pointing problems, Note that for Sessions 5 and 6, the WVR calibrations reduced the post-fit residuals.

The VLBI scan-averaged residual phase delays (i.e. after the least squares fits in MODEST) and WVR station-differenced path delays for Sessions 5 and 6 are shown in Figure 1. The MODEST VLBI solution used for this figure included the estimation and subtraction of a mean tropospheric zenith delay, but did not include WVR calibration. The line-of-sight residual delays (one for each scan) have all been mapped to the zenith, using the factor sin t?, where θ is elevation angle. A linear least squares fit (delay vs. time) has been removed from the zenith WVR delays. This process allows a more valid comparison with the VLB1 residual delays, which have also had a linear delay rate fitted and subtracted. Examination of Figure 1 shows good correlation between the VLB1 and WVR delay changes during some time intervals. However, there are large systematic differences at other times. In order to understand those differences, we examined the VLBI and WVR delay variations in several ways.

The standard deviation of the zenith residuals for VLBI and for single site' and site-differenced WVR zenith delays are given in Table 5. The VLBI values correspond to those plotted in Figures 1 a and lb: line-of-sight values with a clock, clock rate, and mean zenith troposphere removed, and the delays then mapped to zenith. The WVR values had a constant offset and a linear rate removed from the zenith delay values. As in Tables 3 and 4, the WVR results for D2 are based on channel 2 only. If the VI ,BI interscan residuals were dominated by the troposphere, we would expect the WVR site-differenced residuals to be at least as large as the VLBI residuals (equal if the WVR measurement errors were much smaller than the troposphere, and larger otherwise). The scatter in

24

the site differenced WVR delays was significantly less than in the VLBI delays for both Sessions 5 and 6. Over the duration of a session, either the WVRS underestimated the tropospheric variations, or the VLBI measurements had some significant noise source in addition to the troposphere. Because the sites at 1")SS 13 and DSS 15 were nearby and similar, we would expect the individual site WVR standard deviations to be comparable. The fact that the 1)2 residual *rms* values were substantially larger than the J3 residuals suggests that D2 instrument errors contributed significantly to the D2 residuals. The mechanical design of the D WVRs makes them more susceptible to pointing errors than J WVRs. An elevation angle offset for each D2 channel was estimated from tip curves: 0.9° for channel 1 and 0.5° for channel 2. However, because all tip curves during our observations were performed along one azimuth, there was no way to determine the azimuth dependence of these offsets. With an unknown azimuth dependence for both channels, the pointing error for channel 1 was expected to be larger than for channel 2. An elevation error of 0,5° in channel 2 at 30° elevation angle would cause a fractional error of 2%, or ≈ 6 psec for the conditions during these observations. If we assume that the J3 *interscan* scatter is dominated by tropospheric fluctuations rather than by instrument errors, we can multiply the Table 5 J3 values by $\sqrt{2}$ to obtain a 'reduced pointing error' estimate of site-differenced variability. These synthesized site- differenced residuals are 4.2 psec and 7.1 psec for Sessions 5 and 6, considerably less than the VLBI residuals.

B. Intrascan Delay Variability

In order to analyze the delay variations on short ($\leq$ 700 s) time scales, we cal-

culated structure functions from WV R line-of-sight delays and from residual VLB1 phase delays within individual scans (i.e. *intrascan* residuals). For a delay τ measured at time t, the structure function D_τ (At) for a time interval Δt is $D_\tau(\Delta t) \equiv \langle [\tau(t) - \tau(t + \Delta t)]^2 \rangle$. We used long ($\geq 300$ s) scans in this comparison, because these scans provided the largest possible logarithmic range of time interval.

For each of Sessions 5 and 6, WVR structure functions (using individual 5-6 s integrations) were calculated for all long scans, mapped to a reference elevation angle (described below), and averaged. There were four such scans in Session 5 and thirteen in Session 6. The mapping between elevation angles (for both WVR and VLBI structure functions) was determined from numerical integration of the Treuhaft-Lanyi model; it was $\approx \sin\theta_{obs} / \sin\theta_{ref}$, where θ_{obs} is the elevation angle where the structure function was measured and θ_{ref} is the reference elevation angle. The averaged structure function for each WVR was then multiplied by 2, because they were derived from single station data and the VLBI structure functions were derived from station-differenced data.

All long scans in Sessions 5 and 6 had VLB1 elevation angles $\theta_{VLBI > 37°}$ or $< 20°$, For VLBI structure functions, the low elevation angle ($< 20°$) scans could not be used. At these low elevation angles, sidereal tracking causes a significant nonlinear airmass change with time. Combined with imperfectly modeled zenith delays (i. e. the static troposphere), this effect corrupted the measurement of actual fluctuations. (Because the WVRs did not move during observations, their structure functions did not suffer from this problem.) The structure functions (based on residual τ_{ph} **(S/X)** values for 2 s integrations) from all long scans with $\theta_{VLBI} > 37°$ (three in Session 5 and one in Session 6)

were mapped to θ_{ref} and averaged. The reference elevation angle θ_{ref} was the mean VLBI elevation angle for these scans in each session ($\theta_{ref} = 38.5°$ in Session 5 and $\theta_{ref} = 40.3°$ in Session 6).

The WVR and VLBI structure functions are shown in Figures 2a (for Session 5) and 2b (for Session 6). The removal of a best-fit delay rate by FIT suppressed any true variations on time scales longer than approximately half a scan, so that the VLBI structure functions are only shown for intervals < 300s. For Session 6, all but one of the long scans were split in half for WVR pointing, so the averaged WVR structure functions are only shown for At < 350 s in Figure 2b. Except at time scales < 100 s, where thermal noise dominated the WVR structure functions, the VLBI and WVR structure functions show a qualitative agreement.

In Figures 3a and 3b, the VLBI and WVR structure functions are shown on a logarithmic scale. Also shown for comparison is the theoretical Treuhaft-Lanyi structure function for θ_{ref} under typical Goldstone conditions ($C_\chi = 7 \times 10^{-8} m^{-1}3$, the mean Goldstone value derived from intercontinental DSN VLBI observations, 8 m/s wind velocity). The thermal noise floor in both the WVR and VLBI structure functions can be clearly seen. At time scales > 100 s (i.e. where thermal noise is not important), the measured structure functions (for both VLBI and WVRs) are a factor of 2-4 smaller than expected for normal conditions.

C. Session Average VLBI Structure Functions

In order to quantify the average level of tropospheric activity for each session, high SNR scans were used to determine the VLBI structure function.

The measured VLBI D_τ values were compared to theoretical structure functions, based upon the model of Treuhaft and Lanyi (1987), and the results are presented in Table 6. The parameters in the model include elevation angle (chosen to be the same as in the individual VLBI scans), vector wind velocity, tropospheric slab height (chosen to be 2 km, the mean wet tropospheric scale height), and the structure constant C_χ (7 x 10^{-8} m$^{-1/3}$). Vector wind velocities as a function of height were measured by optical tracking of our radiosondes at DSS 13, with launches every 6 hours, The vector wind velocities used in the structure function calculations were linear interpolations (in time) of the values measured by radiosonde tracking.

For each scan, the square root of the ratio of measured to theoretical value of D_τ is given in column 4 of Table 6. The value of At used to determine this ratio was 50s for 700-800s scans and 16 s for 100–150 s scans, as indicated in column 3. These At values were chosen to be large enough to yield negligible contribution from thermal noise, yet be short enough that D_τ was not significantly reduced by the linear delay rate subtraction done by FIT. The quantity in column 4 varies linearly with C_χ. Column 5 gives the mean of the column 4 values for each session. As was evident from Figures 3a and 3b, the magnitude of water vapor fluctuation.. during this experiment was significantly less than normal for Goldstone.

For each session, a corrected value of C_χ was obtained by multiplying the nominal value (7 x 10^{-8} m 1/3) by the mean $\sqrt{D_\tau \ (measured) \ /D, \ (theory)}$ value, The corrected C_χ value represented the mean tropospheric activity, as measured from the *intrascan* residuals. This C_χ value was used to calculate the tropospheric delay st anc.:d deviation $\sigma(T)$ expected for the entire session

28

(*i. e.* the *interscan rms* residual). The variance σ^2 (7') of a random process over an interval T can be expressed in terms of the structure function as (Treuhaft and Lanyi, 1987)

$$(9) \qquad \sigma^2(T) = \frac{1}{T} \int_0^T (T-t) D_{\tau_{2stn}}(t) dt$$

In eq. (9), $D_{\tau_{2stn}}(t)$ is the two-station delay structure function, the expected square of the line-of-sight delay difference at the two sites (DSS 13 and DSS 15). Using a frozen flow model, separations in space and time are related through the vector wind velocity $\vec{v}_w$. Thus, for a time interval At, the vector used for the calculations of $D_{\tau_{2stn}}(t)$ is $\vec{v}_w \Delta t + (\vec{x}_{15} - \vec{x}_{13})$, where $\vec{x}_{15}$ and $\vec{x}_{13}$ are the locations of DSS 15 and DSS 13. For time scales much less than the wind crossing time of the interferometer (i.e. At $<< \|\vec{x}_{15} - \vec{x}_{13}\|/v_w$), variations at the two sites are uncorrelated, and $D_{\tau_{2stn}}(t) \approx 2 D_{\tau_{1stn}}(t)$, where $D_{\tau_{1stn}}(t)$ is the single station delay structure function. This approximation was used for the calculations in Sections Va and Vb. The time scale used in evaluating eq. (9) was the length of a session, and the wind velocity was the mean value measured at 1 km height during that session, Because the scans in each session had a reasonably uniform distribution over any one quadrant of the sky, a source-wind azimuth of 45° was used in these calculations. The dependence of calculated tropospheric effects upon wind velocity is fairly weak. Use of the default wind velocity of 8 m/s changed the estimated tropospheric *interscan rms* by < 20%. For the elevation angle in the model, we used the mean airmass-weighted elevation angle for all VLBI scans in a session which had high quality WVR data at both stations: 42° for Session 4, 47° for Session 5, and 50° for Session 6. The results of these calculations are given in Column 6 of Table 6.

D. Implications of the Model Predictions of *Interscan* VLBI Residuals

A comparison of VLBI-measured and the model-predicted *interscan* residuals is given in Table 7. For each session, the predicted delay *rms* due to the troposphere, based on the VLBI *intrascan* structure functions (column 6 of Table 6) is shown in column 2. The measured VLBI *rms*, with a solution for a mean troposphere, but without WVR calibration (column 2 of Table 4) is given in column 3. The discrepancy between the values in columns 2 and 3 indicates that non-tropospheric (i. e. instrumental) errors were the major source of the VLBI *interscan* delay residuals.

Significant instrumental delay variations at DSS 13 could have remained uncalibrated. Table 8 gives the *rms* phase delay variation (with respect to a least squares linear fit in time) for the instrumental phase calibration measurements at each station for Sessions 4-6, at both S and X-band. The instrumental delay variations at DSS 13 were significantly larger than for DSS 15 during all three sessions. If the phase calibration had worked perfectly, even the larger DSS 13 variations would not pose a problem. However, the DSS 13 phase calibration system was not able to measure delay changes on the transmission from the control room up to the antenna focus, We suspect that these instrumental delay changes constituted the non-tropospheric component of our *interscan rms.* Instrumental delay changes due to mechanical motion of the antenna would likely be much smaller during sidereal tracking than when the antenna slewed from one source to another. Instrumental changes due to thermal variations are likely to be important only over time scales longer than approximately an hour, when significant temperature changes can accumulate.

As a further test of the nature of the VLBI residuals, their elevation angle dependence was examined. For the case where WVR calibration was not applied, the VLBI residuals for some low elevation angle scans were large. When three was a long antenna slew after several scans in a small area of the sky, there was often a substantial change in the residuals. Both of these effects went, away when WVR calibration was applied, suggesting that tropospheric effects (largest at low elevation angles, or when comparing two region.. which are far apart on the sky) had been largely removed. The signature of the VLBI residuals *with* WVR calibration was a systematic variation on time scales > 1 hr, with no obvious elevation angle dependence. We suspect that thermal variations in the DSS 13 antenna or receiver system were the most likely cause of the largest component of the long term (*interscan*) residuals.

If the troposphere model calculations are correct, perfect line-of-sight tropospheric delay calibrations would reduce (in quadrature) the total *rms* (column 3 in Table 7) by the amount in column 2. This 'perfect calibration' *interscan rms* improvement is given in column 4. The measured improvement from WVR calibration is given in column 5. Except for Session 4, the improvement from WVR calibration is a large fraction of the calculated maximum improvement. This shows that WVR measurements were able to calibrate the majority of the wet tropospheric fluctuations. Because of the larger VLBI instrumental effects during Session 4 (see Table 7) and the use of clock breaks in MODEST to reduce their signature, the estimate of the potential improvement from troposphere calibration is more uncertain than for the other sessions.

VI. CONCLUSIONS

31

Application of WVR calibration resulted in a definite but minor (1 %18%) reduction in the VI, BI *interscan rms* residual delays, and is consistent with our understanding of the relative amounts of instrumental and atmospheric fluctuations. We conclude that, over the duration of an observing session, the VLBI residual delays had a larger instrumental component than a tropospheric component, and that the WVR calibration removed most of the tropospheric component of these delays. This conclusion is based upon the following evidence.

1) Within scans, the WVRS and VLBI measured similar levels of delay variations (*intrascan* residuals), as shown by the agreement in their structure functions (Figures 2 and 3). On longer time scales, the VLBI delay residuals were larger than the WVR residuals (Table 5).

2) The VLBI residual values *within* and *between* scans are not consistent. The level of *intrascan* residuals implies that the *interscan* residuals should be a factor of 1.8–2.2 smaller than was actually measured. This is most easily explained by a non tropospheric component to the long time scale VLBI residuals.

3) WVR calibration of VLBI delays reduced the *interscan* residuals by nearly the amount calculated as being due to the troposphere.

4) When the WVR site-differenced residuals are corrected for an apparent pointing error in the D2 unit, the ratio of this synthesized WVR residual zenith delay to the VLBI residual delay (0.39 and 0.68 for Sessions 5 and 6) is close to the ratio of 'predicted troposphere rms' to 'actual (VLBI) *rms*' (columns 2 and 3 in Table 7).

32

Our test of the wet delay calibration ability of WVRs was hindered by the quiet nature of the troposphere during t hese observations. Future tests should be conducted during times (e.g. summer afternoons) when convection-driven atmospheric turbulence is common.

REFERENCES

Boudouris, G. 1963, *J. Res. Nat. Bur. Stand., Sect. D*, 69D, pp. 631-684.

Chandrasekhar, S. 1950, *Radiative Transfer*, University of Chicago Press, Chicago.

Denning, R. F., Guidero, S. L., Parks, G. S., and Gary, B. L., 1989, *J. Geophys. Res.*, 94, No. D14, pp. 16757-16765.

Edwards, C. D. 1990, *JPL Interoffice Memorandum* 335. 1-90-015, Jet Propulsion Laboratory, Pasadena, CA.

Edwards, C. D., Rogstad, D. H., Fort, D. N., White, L., and Iijima, B., *The Telecommunications and Data Acquisition Progress Report, 1992, 42-1* 10, pp. 52-62, Jet Propulsion Laboratory, Pasadena, California.

Elgered, G., 1993, "Tropospheric Radio Path Delay From Ground-based Microwave Radiometry," Chapter 5 in *Atmospheric Remote Sensing by Microwave Radiometry*, edited by M. Janssen, Wiley & Sons.

England, M. N., Schmidlin, F. J., and Johansson, J. M., 1993, *IEEE Trans.' Geoscience and Remote Sensing, 31*, No. 2, pp. 389--398.

Gary, B. L., Keihm, S. J., and Janssen, M. A., 1985, *IEEE Trans. Geoscience and Remote Sensing, GE-23*, pp. 479-484.

Janssen, M. A., 1985, *IEEE Trans. Geoscience and Remote Sensing*, **GE-23**, No. 4, pp. *485--490.*

Hill, R. J., Lawrence, R. S., and Priestly, J. T., 1982, *Radio Science*, 17, pp. 1251-1257.

Keihm, S. J., 1991, "Water Vapor Radiometer Intercomparison Experiment: Platteville, Colorado, March 1-14, 1991 ," JPL Document D-8898, Jet Propulsion Laboratory, Pasadena, California,

Keihm, S. J,, 1992, *Proceedings of a Specialist Meeting on Microwave Radiometry and Remote Sensing Applications,* (E. R. Westwater, eel.), Boulder, CO, pp. 211-218.

Lichten, S. M., 1990, *The Telecommunications and Data Acquisition Progress Report, 42–100, pp.* **1-12,** Jet Propulsion Laboratory, Pasadena, California.

Linfield, R. P., and Wilcox, J. Z., 1993, *The Telecommunications and Data Acquisition Progress Report, 42–1* 14, pp. 1--9, Jet Propulsion Laboratory, Pasadena, California.

Lowe, S. T. 1992, "Theory of Post-Block 11 VLBI Observable Extraction," JPL Publication 92-7, Jet Propulsion I laboratory, Pasadena, CA.

Owens, J. C., 1967, *Applied Optics, 6, pp. 51-58.*

Resch, G. M., Hogg, D. E., and Napier, P. J., 1984, *Radio Science,* **19,** PP. *411-422.*

Rogers, A. E. *et* al. 1983, Science, 219, 51.

Sigman, E. H. 1987, *The Telecommunications and Data Acquisition Progress Report, 42–92,* pp. 89 104, Jet Propulsion Laboratory, Pasadena, California.

Severs, O. J. 1991, "Observation Model and Parameter Partials for the JPL VLBI Parameter Estimation Software 'MODEST' -– 1991 ," JPL Publication 83--39, Rev. 4, Jet Propulsion laboratory, Pasadena, CA.

Thayer, G. D., *1974, Radio Science, 9, pp. 803-807.*

Tralli, D. M., and Lichten, S. M. 1990, *Bull. Geod.,* 64, pp. 127-159.

Treuhaft, R. N., and Lanyi, G. E., 1987, *Radio Science, 22,* pp. 251-265.

Treuhaft, R.. N., and Lowe, S. '1'., 1991, *The Astronomical Journal, 102,* pp. 1879-1888.

Westwater, E. R., Snider, J. B., and Falls, M. J., 1990, *IEEE Trans. Antennas Propag., AP–38,* pp. *1569 1580.*

Westwater, E. R., 1993, "Ground-Bawd Microwave Remote Sensing of Meteorological Variables," Chapter 4 in *Atmospheric Remote Sensing by Microwave Radiometry,* edited by M. Janssen, Wiley & Sons.

36

Table 1

VLBI Observing Dates, 1993

Session	Start Day	Start UT	Duration
1	*112*	05:10	*5.7* hr
2	116	04:10	**6.7** hr
3	122	05:30	**28.8** hr
4	128	16:50	24.0 hr
5	130	04:50	5.2 hr
6	131	04:20	5.7 hr

Table 2

"

.

Quantity of Usable Data From Each Session

Session	Number of Usable Scans
1	0
2	**0**
3	**0**
4	87
5	46
6	33

Table 3

VLBI *Interscan rms* Residuals Without Mean Zenith Troposphere Estimate

Session	No WVR Calibration	Dual Channel for J3 Channel 2 for D2
4	**20.4** psec	**20.7** psec
5	23.4 psec	16.8 psec
6	19.6 psec	13.7 psec

Table 4

VLBI *Interscan rms* Residuals With Mean Zenith Troposphere Estimate

Session	No WVR Calibration	Dual Channel for J3 Channel 2 for D2
4	**21.0** psec	20.8 psec
5	15.0 psec	13.0 psec
6	18.5 psec	15.1 psec

Table 5

VLBI and WVR *Interscan rms* Zenith Delay Residuals

Session	VLBI	WVR: Site Difference	J3	D2
5	10.7 psec	8.5 psec	3.0 pscc	8.4 psec
6	10.4 psec	6.4 psec	5.0 pscc	8.0 psec

Table 6

Measured and Theoretical Delay Structure Functions

Session	Scan	Δt used for D_τ	$\sqrt{\dfrac{D_\tau\,(\text{measured})}{D_\tau\,(theory)}}$	Mean Value	Predicted *Interscan* *rms* Residual
4	11	16 s	0.48		
	35	16 S	0.80		
	145	16 s	0.54		
	160	16 s	0.40		
	199	16 S	0.16		
	212	16 S	0.29		
	237	16 s	0.17		
	276	16 S	0.23		
	309	16 S	0.28		
				0.37	9.7 psec
5	2	50 s	0.32		
	12	16 S	0.26		
	27	16 S	0.30		
	33	50 s	0.27		
	40	16 S	0.48		
	60	16 S	0.51		
	65	50 s	0.32		
				0.35	8.1 psec
6	4	50 s	0.48		
	8	16 S	0.34		
	20	16 S	0.48		
	35	16 S	0.37		
	38	50 s	0.95		
	54	16 S	0.34		
	59	50 s	0.20		
				0.45	10.2 psec

Table 7

Comparison of Expected and Actual VLBI Residual Delay Improvement from WVR Calibration

Session	Predicted Tropospheric *Interscan rms*	Actual VLBI *7-ins*	Expected *rms* Reduction from Perfect Tropospheric Calibration	Actual *rms* Reduction from WVR Calibration
4	9.7 psec	21.0 psec	11%	1%
5	8.1 psec	15.0 psec	16%	13%
6	10.2 psec	18.5 psec	17%	18%

Table 8

RMS Phase Delays (one delay per scan) Prom Phase Calibration

Session	DSS 13 S-band	DSS 13 X-band	DSS 15 S-band	DSS 15 X-band
4	181 psec	167 psec	8 psec	9 psec
5	10 psec	11 psec	4 psec	4 psec
6	29 psec	30 psec	7 psec	4 psec

FIGURE CAPTIONS

Figure 1

VLBI *interscan* phase delay residuals and WVR delay estimates. All measurements have been mapped to zenith, and have had a linear trend (in time) removed. A mean tropospheric zenith delay has been subtracted from the VLIN data.

a) Session 5

b) Session 6

Figure 2

VLBI and WVR *intrascan* structure functions, shown on a linear scale.

a) Session 5. The curve labeled 'VLBI(avg)' is the average of the VLBI structure functions for the three long ($\geq$ 600 s) scans at elevation angles >30°. The curves labeled 'J3 (avg)' and 'D2 (avg)' are the averages of the J3 and D2 WVR structure functions for all 4 long scans. All structure functions have been scaled to a constant elevation angle (38. 5°, the average elevation angle of the 3 VLBI scans) before averaging. The WVR structure functions have been multiplied by 2 for comparison with the two-station VLBI structure functions. At time scales less than $\sim$ 100 s, the WVR structure functions (especially for J3) are dominated by thermal noise. The VLB1 structure function is not shown for time scales > 300 s, because the least squares delay rate fitting performed on the data has suppressed the structure function in this regime.

b) Session 6. For this session, there was only one long VLB1 scan at elevation angle > 30°, and 13 WVR scans. The WVR structure functions were mapped to the

VLBI elevation angle of 40.3° before averaging. Because only one WVR scan was longer than 300 s, the WVR structure functions are only shown for 0–300 s.
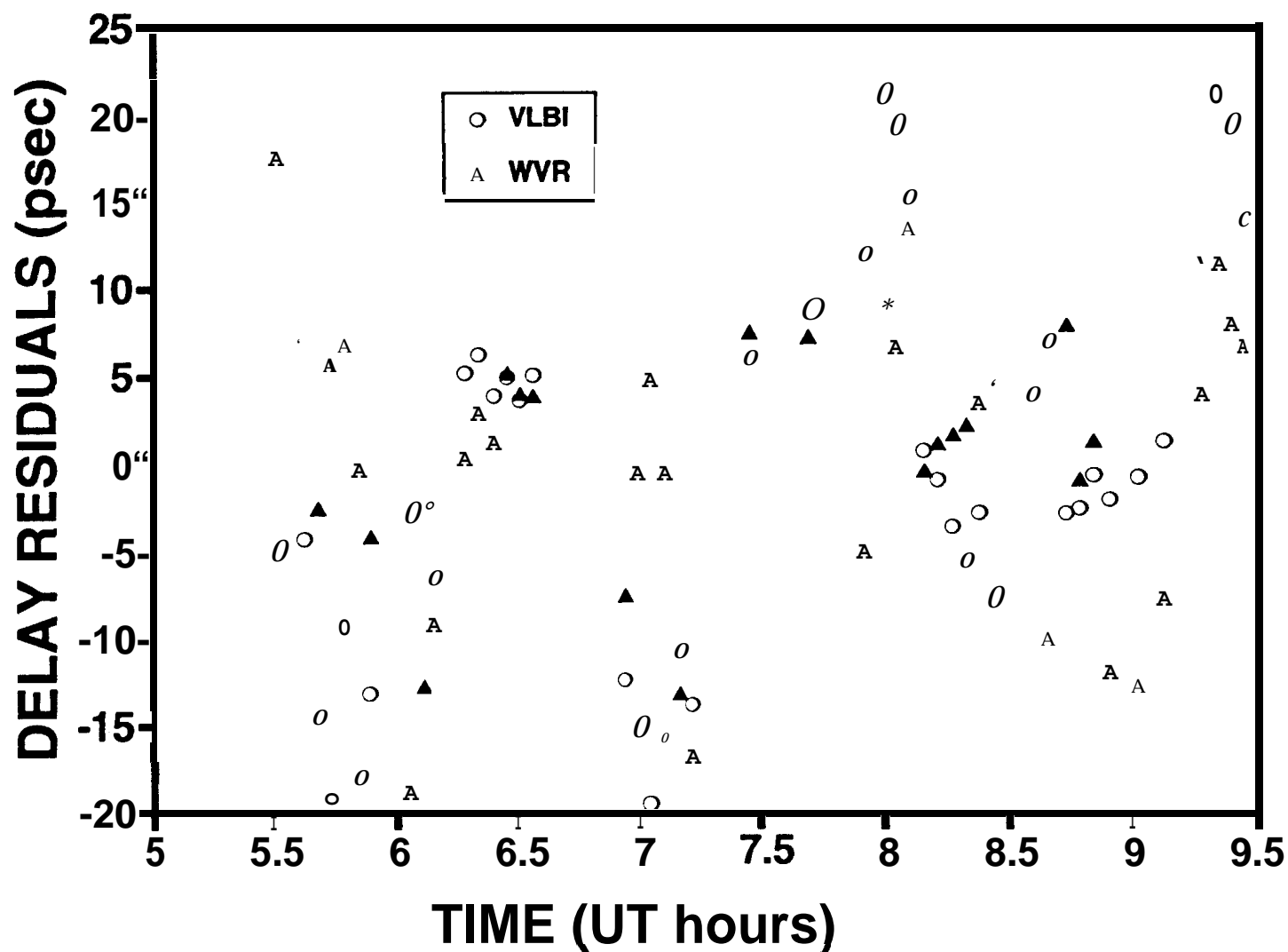

Figure 3

VLB1 and WVR structure functions shown on a log scale. The theoretical Treuhaft-Lanyi structure function for average Goldstone tropospheric conditions $(C_x = 7 \times 10^{-8}\,m^{-/3})$ is shown for comparison. The VLBI structure function is dominated by thermal noise on time scales less than ~ 10 s.

a) Session 5

b) Session 6

DAY 130 VLBI and WVR
ZENITH DELAY RESIDUALS

Fig 1a)

DAY 131 VLBI and WVR
ZENITH DELAY RESIDUALS
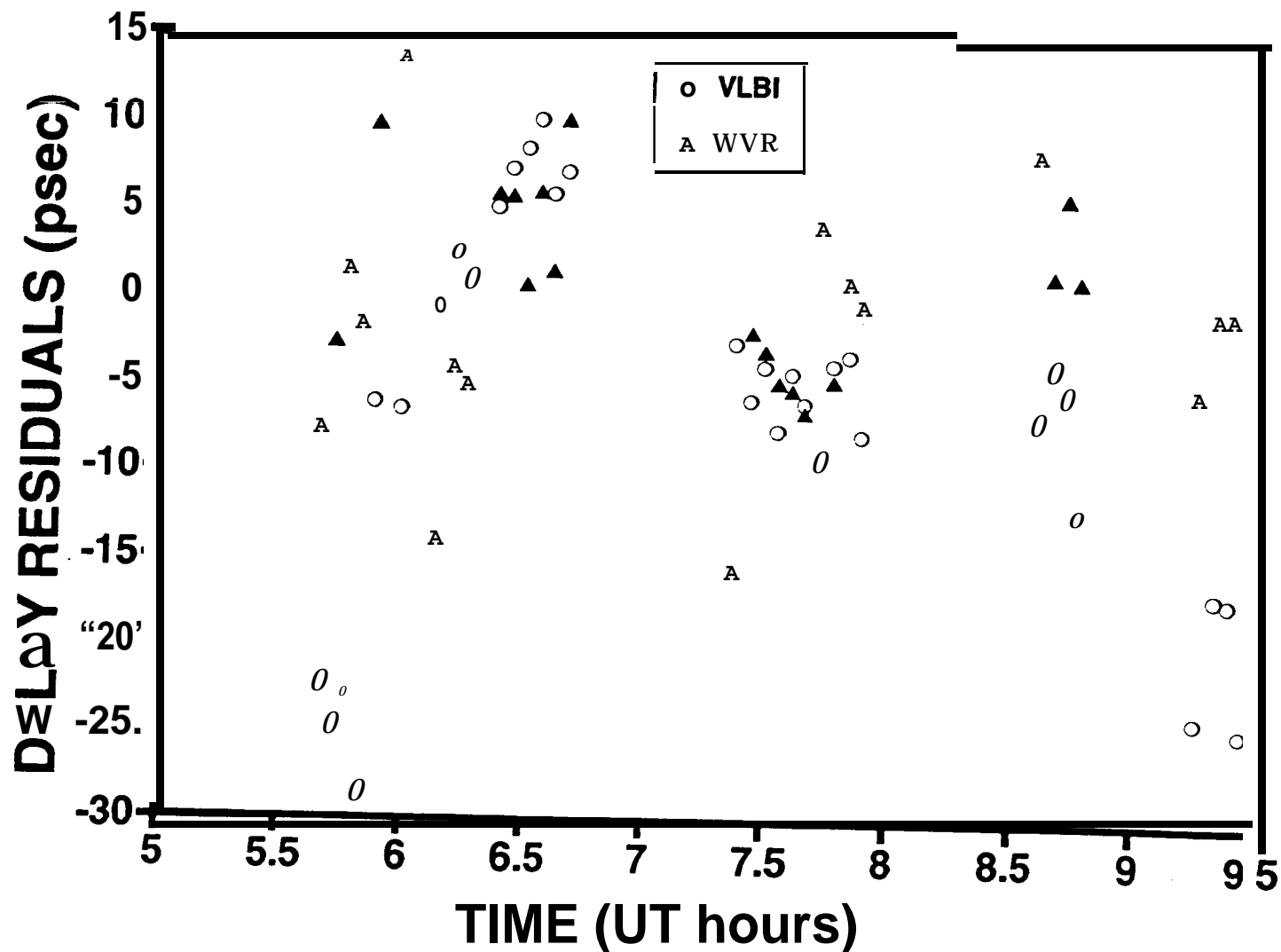
Fig 1b)
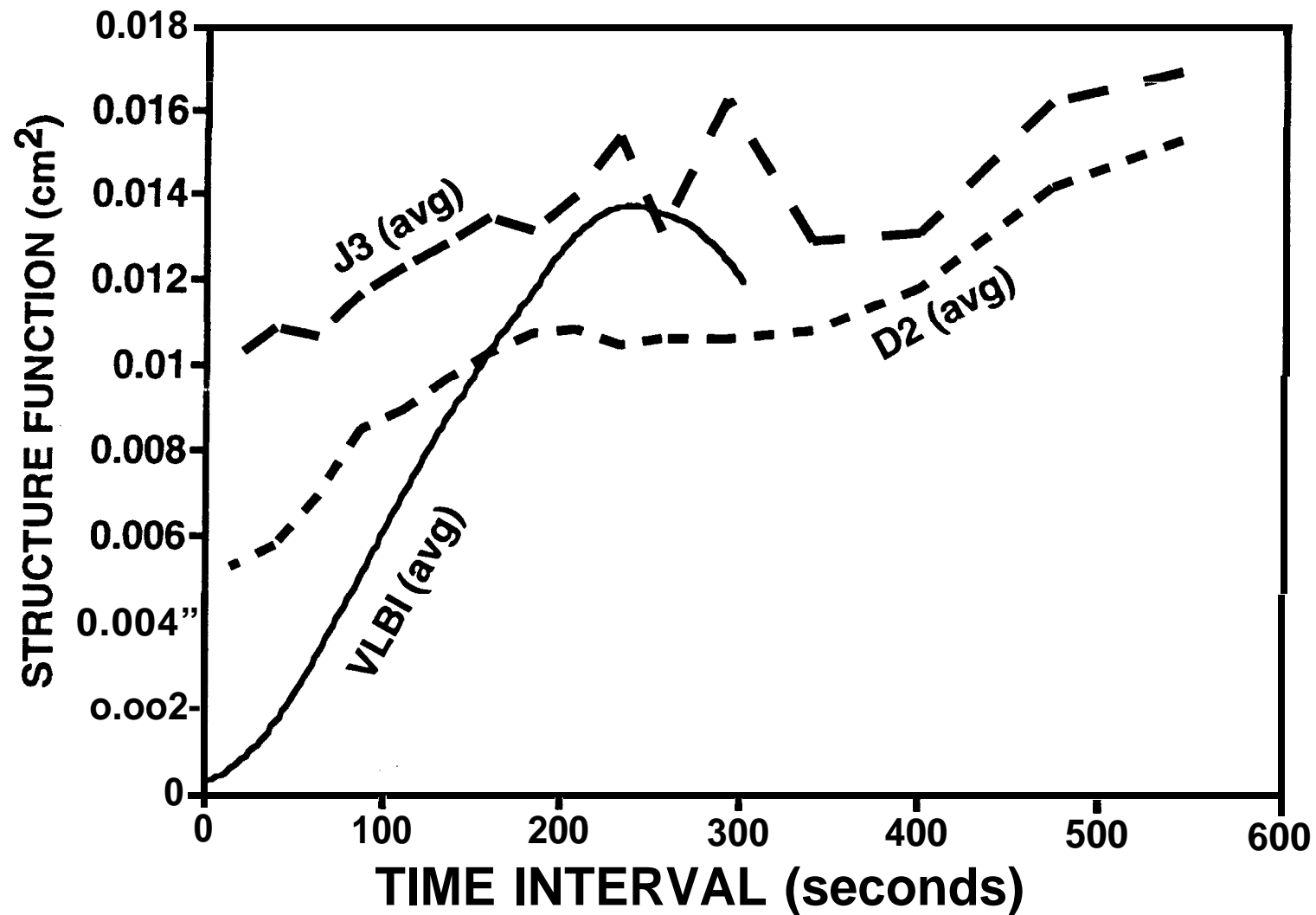
SESSION 5 INTRASCAN STRUCTURE FUNCTIONS
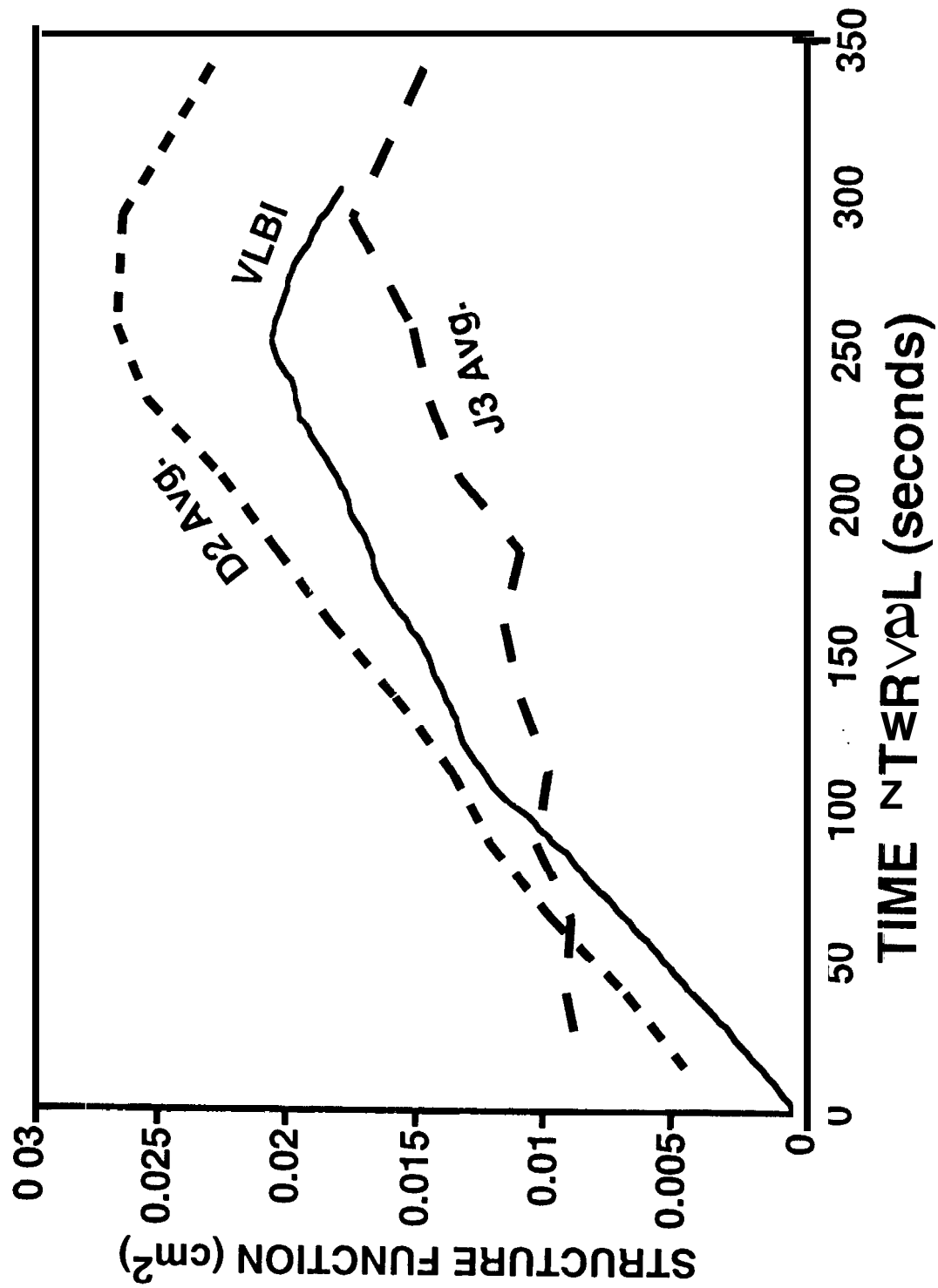
Fig 2b)

SESSION 6 INTRASCAN STRUCTURE FUNCTIONS

SESSION 5 INTRASCAN STRUCTURE FUNCTIONS
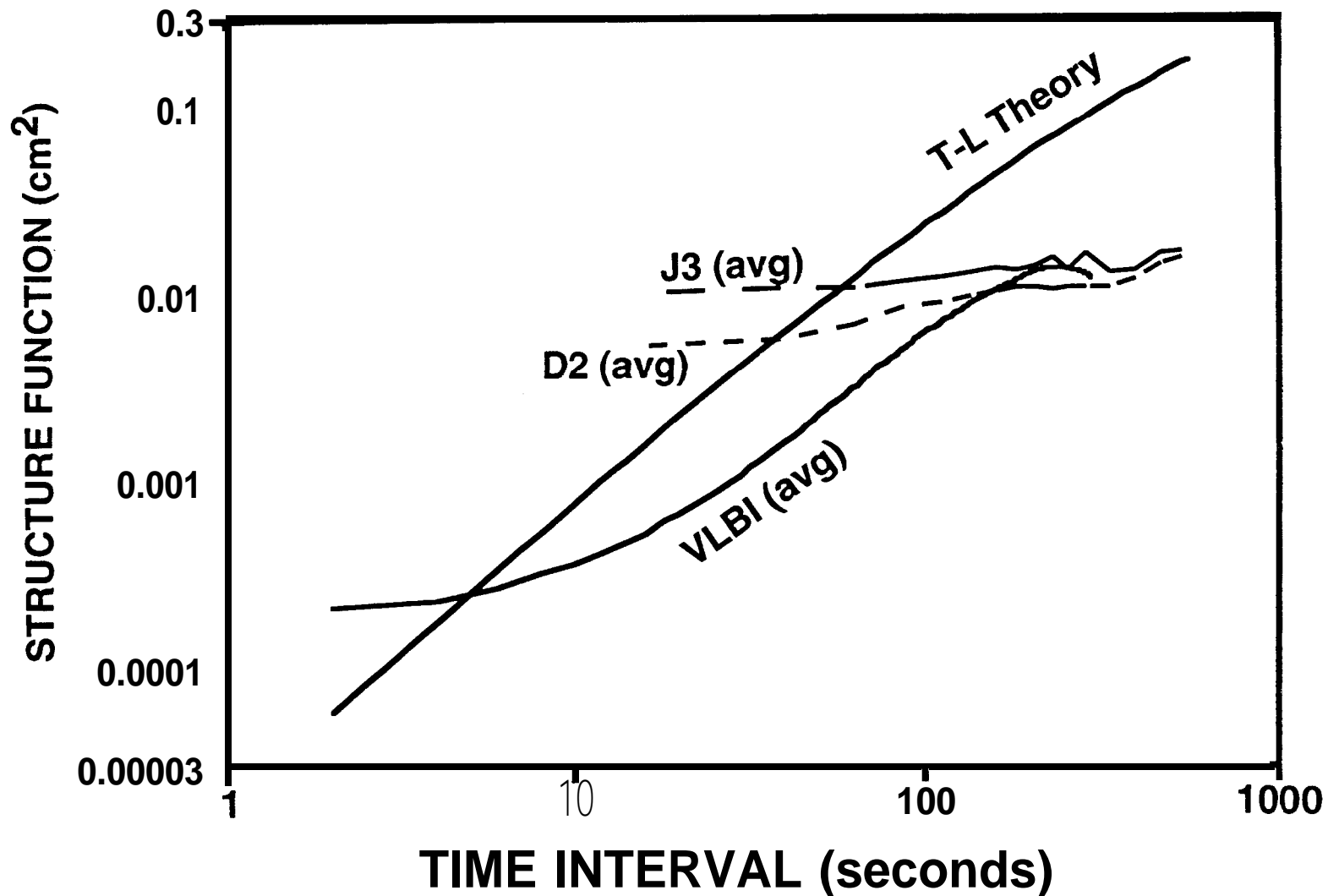
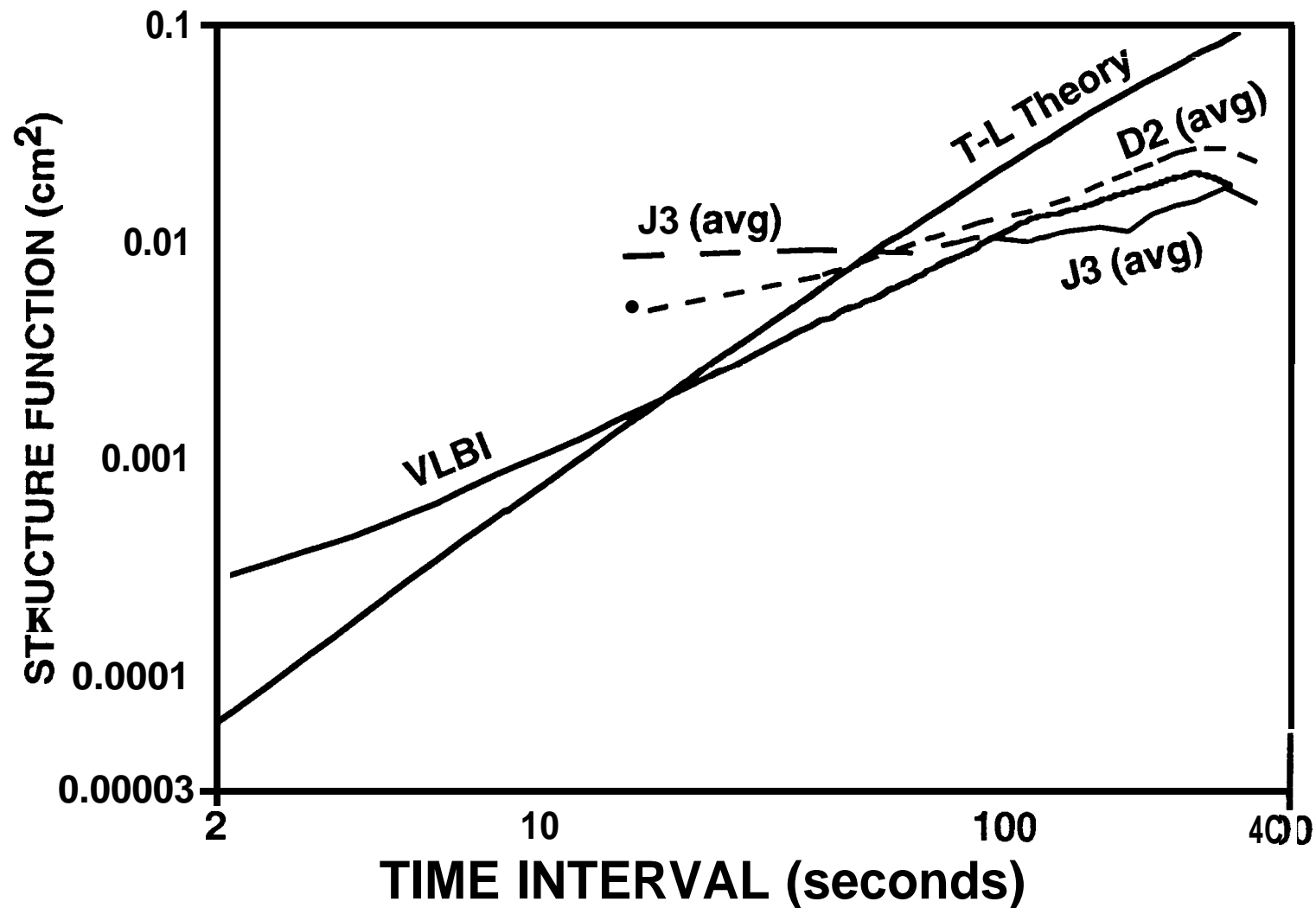Fig 3a

SESSION 6 INTRASCAN
STRUCTURE FUNCTIONS